Coexistence of antiferromagnetic cubic and ferromagnetic tetragonal polymorphs in epitaxial CuMnSb films

A. Ciechan,[1] P. Dłużewski,[1] S. Kret,[1] K. Gas,[1,2] L. Scheffler,[3,4] C. Gould,[3,4] J. Kleinlein,[3,4] M. Sawicki,[1,5,*] L. W. Molenkamp,[3,4] and P. Bogusławski[1,†]

[1]*Institute of Physics, Polish Academy of Sciences, Aleja Lotnikow 32/46, PL-02668 Warsaw, Poland*
[2]*Center for Science and Innovation in Spintronics, Tohoku University, Sendai 980-8577, Japan*
[3]*Physikalisches Institut (EP3), Universität Würzburg, 97074 Würzburg, Germany*
[4]*Institute for Topological Insulators, Universität Würzburg, 97074 Würzburg, Germany*
[5]*Research Institute of Electrical Communication, Tohoku University, Katahira 2-1-1, Aoba-ku, Sendai 980-8577, Japan*

(Received 20 May 2024; revised 8 July 2024; accepted 10 July 2024; published 25 July 2024)

High-resolution transmission electron microscopy and superconducting quantum interference device magnetometry shows that epitaxial CuMnSb films exhibit a coexistence of two magnetic phases, coherently intertwined in nanometric scales. The dominant α phase is half-Heusler cubic antiferromagnet with the Néel temperature of 62 K, the equilibrium structure of bulk CuMnSb. The secondary phase is its ferromagnetic tetragonal β polymorph with the Curie temperature of about 100 K. First principles calculations provide a consistent interpretation of experiment, since (i) total energy of β–CuMnSb is higher than that of α–CuMnSb only by 0.12 eV per formula unit, which allows for epitaxial stabilization of this phase, (ii) the metallic character of β–CuMnSb favors the Ruderman-Kittel-Kasuya-Yoshida ferromagnetic coupling, and (iii) the calculated effective Curie-Weiss magnetic moment of Mn ions in both phases is about 5.5 μ_B, favorably close to the measured value. Calculated properties of all point native defects indicate that the most likely to occur are Mn_{Cu} antisites. They affect magnetic properties of epilayers, but they cannot induce the ferromagnetic order in CuMnSb. Combined, the findings highlight a practical route towards fabrication of functional materials in which coexisting polymorphs provide complementing functionalities in one host.

DOI: 10.1103/PhysRevB.110.014436

I. INTRODUCTION

One of the most challenging and long-standing problems in fundamental magnetism is a competition between ferromagnetic and antiferromagnetic phases. Their interplay at the interface results in a well-known effect of the exchange bias [1,2], which fuels now a rapid development of spintronics [3] and unconventional computing [4]. The material class of Heusler alloys was previously used to study the origin of the transition between magnetic phases because it offers a wide spectrum of functionalities [5]. Indeed, Heusler alloys exhibit ferromagnetic (FM), antiferromagnetic (AFM), and canted ferromagnetic order. This indicates that different types of magnetic coupling are competing in this family. Moreover, some of its members display structural polymorphism, which allows studying relationships between the crystalline phase, the magnetic phase, and the corresponding electronic structure.

Heusler alloys incorporate full-Heusler (X_2YZ) and half-Heusler (XYZ) variants, where X and Y stand for transition metals, whereas Z denotes anions from the main group. In this class, qualitative changes in material characteristics can be achieved by chemical substitution on either the transition metal cation or on the anion sublattice. Typically, the change of the cation does not change the crystal structure, but it can induce a crossover between the AFM and the FM magnetic phases. A rarely met complete solubility with only marginally affected crystallinity of the otherwise chemically homogenous systems allowed to study the FM-AFM phase competition in detail. The prominent examples are quaternary solid solutions such as $Ru_2Mn_{1-x}Fe_xSn$ [6–8] Heuslers, and $Co_{1-x}Ni_xMnSb$ [9,10], $Cu_{1-x}Ni_xMnSb$ [11–13], $Co_{1-x}Cu_xMnSb$ [14], and $Cu_{1-x}Pd_xMnSb$ [15] half-Heuslers. In the latter case, the crossover between AFM to FM phases is related to a change in the electronic structure from semimetallic to half-metallic [16,17].

Cu–based CuMnZ compounds are antiferromagnets. This feature attracts attention given the recent progress achieved in the AFM spintronics [18]. Of particular interest is CuMnAs, with a high Néel temperature $T_N = 480$ K [19]. In this case, features essential for applications, such as anisotropic magnetoresistance [20,21], current-induced electrical switching of the Néel vector [22] and of the magnetic domains [23], have been demonstrated.

The AFM order of CuMnZ is independent of the actual crystalline structure. The equilibrium structure of bulk CuMnP and CuMnAs is orthorhombic, while that of CuMnSb is half-Heusler cubic, referred to below as the α phase. However, epitaxial growth can stabilizes metastable phases. This is the case of epitaxial layers of CuMnAs, grown on both GaP

*Contact author: mikes@ifpan.edu.pl
†Contact author: bogus@ifpan.edu.pl

[19–21,24,25] and GaAs [23] substrates, which crystalize in the tetragonal structure, referred to below as the β phase. Theoretical investigations of the crystalline properties of CuMnZ series show that the total energy difference between the cubic and orthorhombic phase is about 1 eV per formula unit (f.u.) for CuMnP, and about 0.5 eV per f.u. for CuMnAs [26]. This suggests that the orthorhombic phase of CuMnSb, the last member of the CuMnZ series, may not be stable, and indeed the stable structure is the α phase. However, as we show here, epitaxial stabilization of CuMnSb in the β phase is in principle possible, because the calculated energy difference between α–CuMnSb and β–CuMnSb is small, about 0.12 eV per f.u. Moreover, the β–CuMnSb polymorph becomes stable at pressures above 7 GPa [27].

Concerning the magnetic properties, the Néel temperature of both orthorhombic CuMnAs and β–CuMnAs is well above the room temperature [19], whereas that of α–CuMnSb is lower, about 60 K [28,29]. Theory agrees with experiment, since according to Ref. [30], in the orthorhombic CuMnP and CuMnAs, the AFM order is more stable than the FM by about 250 meV/Mn. This energy difference is smaller in the cubic phase of CuMnZ compounds, for which the AFM order is lower in energy than FM one by about 50 meV per f.u. [30,31] Finally, the AFM order of α–CuMnSb is stable under applied magnetic field, as T_N does not change up to 50 Tesla [32].

Turning to the electronic structure of the CuMnP-CuMnAs-CuMnSb series we observe that the character of the energy band gap depends on the anion. Similar to the case of, e.g., zinc blende semiconductors, the band gap decreases with the increasing atomic number of the anion [30]. Indeed, CuMnP is a semiconductor, CuMnAs has a practically vanishing band gap, and CuMnSb is a semimetal [33].

Here we experimentally confirm a puzzling coexistence of AFM and FM phases in epitaxial stoichiometric CuMnSb films, observed by us previously [34], and explain the underlying mechanism responsible for this effect. A fine analysis of transmission electron microscopy (TEM) images, Sec. II B, points to the formation of tetragonal β–CuMnSb inclusions embedded coherently within the cubic α–CuMnSb host. The tetragonal structure of these inclusions is the same as that of the tetragonal β–CuMnAs. Magnetic properties of our films, Sec. II C, demonstrate coexistence of two magnetic phases: apart from the dominant AFM one, expected for CuMnSb, the measurements reveal the presence of a FM contribution. This is an unexpected feature within the CuMnZ series, exhibiting the AFM order.

In Sec. III, we employ calculations based on the density functional theory to assess properties of CuMnSb films. In agreement with the experiment, β–CuMnSb is weakly metastable, but its magnetic ground state is FM. Band structures of α and β polymorphs are close, but changes in the density of states at the Fermi level account for the change of the dominant mechanism of the magnetic coupling from AFM superexchange to FM Ruderman-Kittel- Kasuya-Yoshida (RKKY). Finally, in Sec. III E native point defects in CuMnSb are examined to assess their possible influence on the magnetic properties [35]. Our results indicate that the dominant native defects in α–CuMnSb are Mn antisites, and their presence in the films can possibly account for small differences between the measured and the calculated magnetic characteristics, but they do not stabilize the FM order of α–CuMnSb.

II. EXPERIMENTAL RESULTS

A. Experimental Methods

1. Growth conditions

CuMnSb layers about 200-nm thick are grown by molecular beam epitaxy. Separate growth chambers connected by an ultrahigh vacuum transfer system are used for the growth of the individual layers. Low tellurium-doped epiready GaSb (001) wafers are used as substrates. Prior to the growth, the natural oxide layer is desorbed in an Sb atmosphere. Then, 150-nm-thick GaSb buffer layers are grown on the substrates to ensure a high-quality interface for the growth of CuMnSb. The GaSb buffer layers are grown at a substrate temperature of 530°C and a beam equivalent pressure of 4.0×10^{-6} mbar and 5.3×10^{-7} mbar for Sb and Ga, respectively. Sb supply is facilitated by a single-filament effusion cell, while Ga is provided by a double-filament effusion cell.

A substrate temperature of 250°C is used for the growth of CuMnSb films. The corresponding beam equivalent pressures are as follows: $\mathrm{BEP_{Cu}} = 5.80 \times 10^{-9}$ mbar, $\mathrm{BEP_{Mn}} = 9.03 \times 10^{-9}$ mbar, and $\mathrm{BEP_{Sb}} = 4.23 \times 10^{-8}$ mbar. Cu is supplied by a double filament effusion cell, while Mn and Sb are supplied by single filament effusion cells. Following the growth of CuMnSb, a 2.5-nm-thick layer of Al_2O_3 is deposited on the samples through a sequential process of aluminum DC magnetron sputtering and oxidation. Please, refer to Ref. [29] for a comprehensive analysis of the growth process and physical properties of the CuMnSb layers produced using the methodology outlined above.

2. Transmission electron microscopy

Specimens for the transmission electron microscopy (TEM) investigations are prepared by the focused ion beam method in the form of lamellas cut along the [100] and [110] directions, i.e., perpendicularly to the surface (001) plane. Titan Cubed 80-300 electron transmission microscope operating with accelerating voltage 300 kV and equipped with energy-dispersive X-ray spectrometer (EDXS) is used for the study. Most of the investigations are done on Cu grids, but for EDXS elemental analysis a Mo grid is used to avoid interference of Cu fluorescence signal from the grid. This analysis yields percentage atomic concentration at 37(3) : 32(5) : 31(7) for Cu, Mn, and Sb, respectively, which, within the experimental errors (given in the parentheses), correspond to the expected stoichiometric ratio of 33 : 33 : 33.

3. SQUID Magnetometry

Magnetic characterization is performed in a commercial superconducting quantum interference device (SQUID) magnetometer MPMS XL7. The magnetic moment of antiferromagnetic layers is generally very weak and by far dominated by the magnetic response of the bulky semiconductor substrates. Therefore, to counteract the typical shortcomings of commercial magnetometers built around superconducting magnets [36] and to minimize subtraction

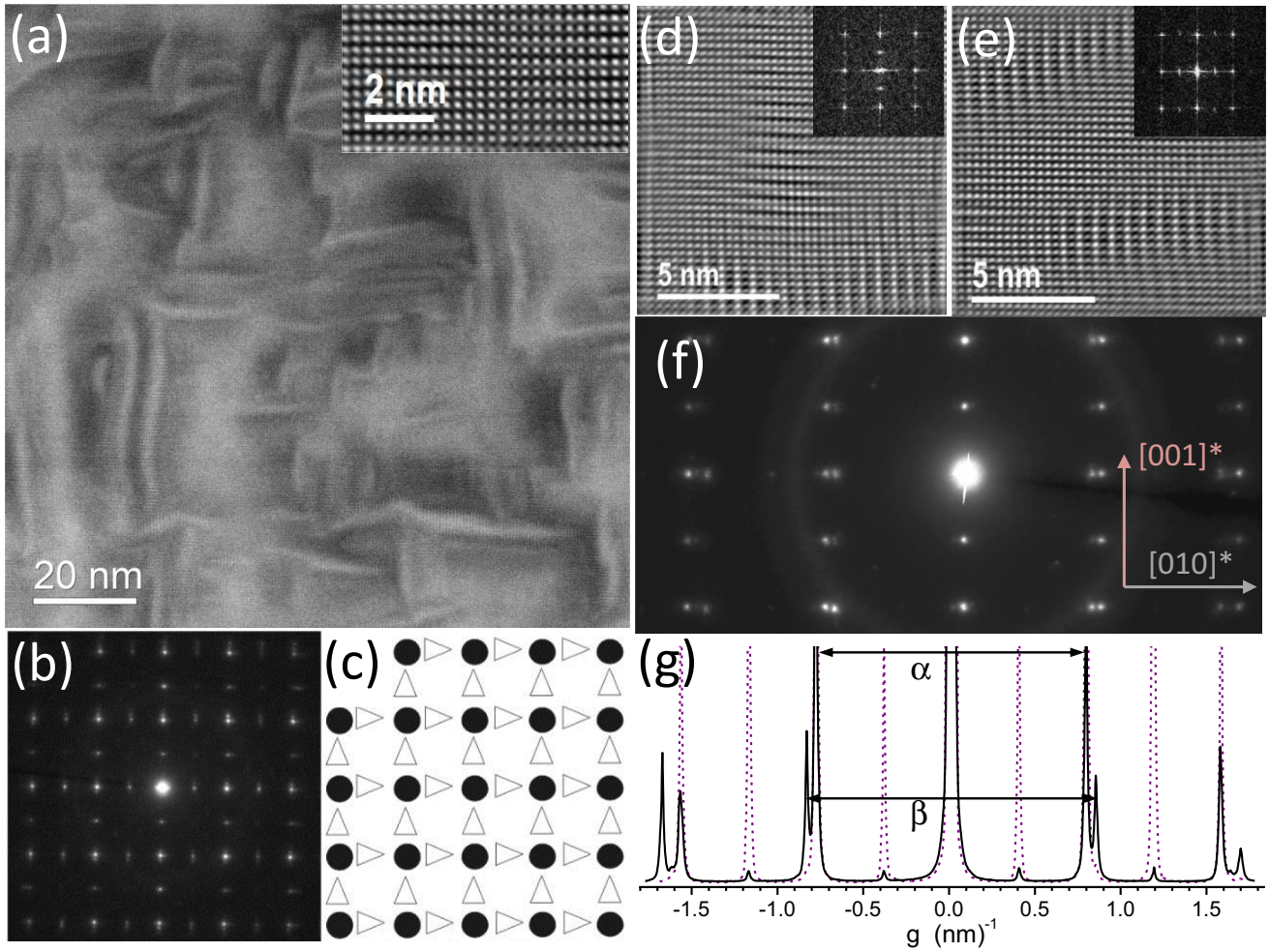

FIG. 1. (a) High-angle annular dark-field scanning transmission electron microscopy image of a CuMnSb layer in the [100] zone axis. The inset in the top-right corner brings up a part of the image in atomic resolution, where bright dots represent columns of Mn and Sb atoms. (b) Electron diffraction pattern of the layer. (c) Schematics of the positions of Bragg's spots from (b). Big bullets represent the main reflections from the cubic CuMnSb structure, whereas the open triangles mark the positions of the weak extra reflections. The orientation of the triangles follows from the analysis of the data in panels (d–g). (d, e) Blown up two regions from panel (a), in which either vertical or horizontal strips dominate. The corresponding Fourier transforms are showed in the top right corners of both panels. (f) Selected area electron diffraction pattern taken at the regions dominated by the vertically oriented strips. (g) Diffraction intensity profiles taken along the horizontal [010]* and the vertical [001]* lines passing through the center the diffraction pattern. The solid line corresponds to the horizontal [010]* direction and the dashed one to the vertical [001]* one in panel (f). Stars denote directions in the reciprocal space. The arrows α and β indicate the length of α–2g(002) and β–2g(002) diffraction vectors, respectively.

errors during data reduction we actively employ the *in situ* compensation [37]. It allows us to reduce the coupling of the signal of the substrates to about 10% of their original strength. The actual effectiveness of the compensation depends on the mass of the sample and its orientation with respect to the SQUID pick-up coils [36,38]. We also strongly underline the importance of a thorough mechanical removal of the metallic MBE glue from the backside of the samples for any magnetic studies. Its strongly nonlinear magnetic contribution can be of the same magnitude as that of the layer of interest [39]. To accurately establish the magnitude of magnetic moment specific to CuMnSb we measure a reference sample grown without the CuMnSb layer [29] using the same sample holder and following exactly the same experimental sequence as that executed for the investigated samples.

B. Structural characterization

An exemplary atomic resolution high-angle annular dark-field scanning transmission electron microscopy (HAADF/STEM) image obtained for the [100] zone axis (the direction of the projection) is in Fig. 1(a). It confirms a high-quality cubic constitution of the material, as it is underlined in the inset. However, at the contrast chosen here, the image in this field of view reveals the presence of stripelike features, which are the main subject of this analysis. In this image, the apparent lengths and widths of the strips are about 40 nm and about 4 nm, respectively, running predominantly either vertically or horizontally in this particular projection. On other images, the strips exhibit a relatively wide distribution of lengths in the 10–100 nm window. Since similarly distributed shadowy stripes are

observed also in the [110] zone axis, we conclude that they form along all three principal crystallographic directions without any particular preferences. The expected $F\bar{4}3m$ cubic structure of α–CuMnSb is clearly confirmed by the fourfold symmetry of the dominant (bright) spots seen on electron diffraction pattern presented in Fig. 1(b).

Importantly, the diffraction pattern in Fig. 1(b) contains also a second set of much fainter reflections, situated halfway between two adjacent reflections of the main pattern. This indicates the presence of a second crystallographic β phase, which periodicity in the corresponding direction is doubled relative to that of α–CuMnSb, but otherwise coherent with this host structure. We bring all the Bragg's spots up in Fig. 1(c), in which the bullets represent the main reflections from α–CuMnSb, whereas the open triangles mark the positions of the weak ones, which are forbidden for this structure.

The presence of β–CuMnSb is further substantiated by the inspection of the two close-ups from Fig. 1(a), shown in Figs. 1(d) and 1(e). At this magnification they reveal that, on top of the otherwise cubic arrangement of atomic columns, the strips' brightness alternates every second {002} plane along the direction perpendicular to strip's long axis. The modulation is vertical in Fig. 1(d), whereas it goes horizontally in Fig. 1(e). The top right corners of these figures contain the corresponding Fourier transform of the parent image, and, similarly to Fig. 1(b), both patterns are dominated by the main reflections of α–CuMnSb. The additional spots are embedded either along vertical [Fig. 1(d)] or horizontal [Fig. 1(e)] lines, i.e., the presence of vertical and horizontal orientations is mutually exclusive. This feature is reflected in Fig. 1(c), where the additional spots are marked by differently oriented triangles. The triangles with apexes directed vertically correspond to the vertical orientation of the brightness modulation in Fig. 1(d), whereas the horizontal direction of apexes corresponds to the horizontal modulation.

Based on the data shown above we propose that the second phase of CuMnSb, present in our films in the form of strips, is a tetragonal structure, which also is the structure of epitaxial CuMnAs [19–21,23–25], and of CuMnSb at high pressures [27]. This β–CuMnSb polymorph is shown in Fig. 2(b). The difference between α and β phases consists in the location of Cu ions: in the α phase every (001) plane between two consecutive MnSb planes is half-occupied by Cu, whereas in the β phase Cu ions completely fill up every second (001) plane, and the overall stoichiometry of the material is preserved.

Details regarding β–CuMnSb can be inferred from selected area electron diffraction (SAED) patterns taken at regions with different orientations of the strips. Diffraction pattern of an area dominated by the vertically oriented strips is shown in more detail in Fig. 1(f). In agreement with the Fourier transforms, SAED shows the occurrence of specific reflections corresponding to this particular orientation. The reflections common to both the cubic α and the tetragonal β polymorphs are split along the [010]* direction, i.e., orthogonal to the strip's axis, whereas the weak spots of the β phase are not split and are commensurate with the cubic phase. (A star denotes a direction in the reciprocal space.)

We quantify the effect analyzing intensity profiles taken along lines passing through the center of diffraction. The profiles are superimposed, and presented in Fig. 1(g). The

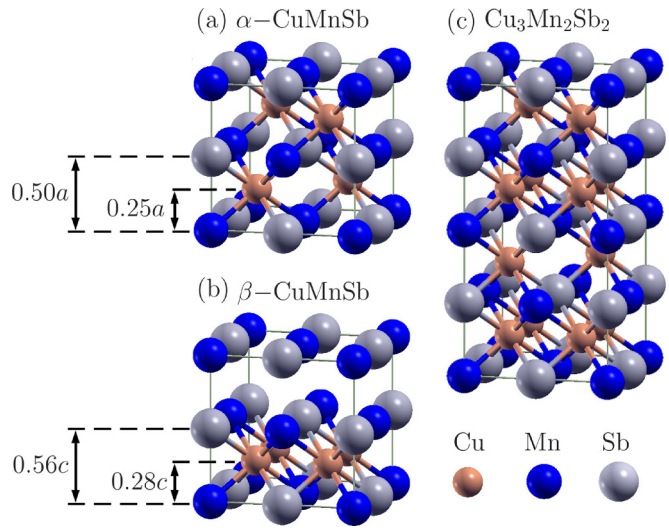

FIG. 2. Crystal structures of (a) α–CuMnSb with the cubic lattice constant a, (b) tetragonal β–CuMnSb with the lattice constants a in the (x, y) plane and c in the [001] direction, and (c) $Cu_3Mn_2Sb_2$.

profile along the [001]* direction reflects the periodicity of α–CuMnSb, while that along [010]* is additionally split. From the figure it follows that in our specimens the c lattice parameter of the β–CuMnSb strips is equal to that of the host α–CuMnSb, 6.2(1) Å, whereas the a and b parameters of the β phase, 5.8(1) Å, are smaller by about 7%. Analogous features are observed for the [010]-oriented strips.

The existence of such a significant strain is confirmed by the calculation of strain maps. We apply the geometrical phase analysis method [40] for the main image presented in Fig. 1(a), and the results are presented in Figs. 3(a) and 3(b) for the horizontal, ϵ_{xx}, and the vertical, ϵ_{zz}, components of strain, respectively. It is seen that stripes' strain is negative (dark shade) perpendicular to strips and almost zero along the strips. For example, on the horizontal strain map [Fig. 3(a)] only vertical strips are visible because they are compressed horizontally, whereas the horizontal strips are invisible because they are not deformed in the horizontal direction.

STEM/HAADF Fourier filtered images of the layer allow us to estimate volume fraction of the β phase. Assuming a cuboid shape of the stripes and their uniform distribution

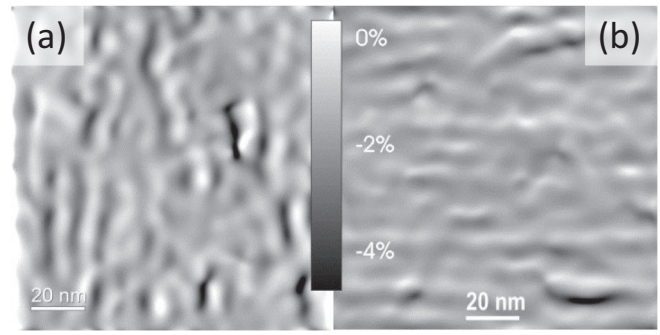

FIG. 3. Strain maps of image shown in Fig. 1(a). (a) The horizontal component of strain ϵ_{xx} and (b) the vertical one, ϵ_{zz}. Geometrical phase analysis method has been applied [40].

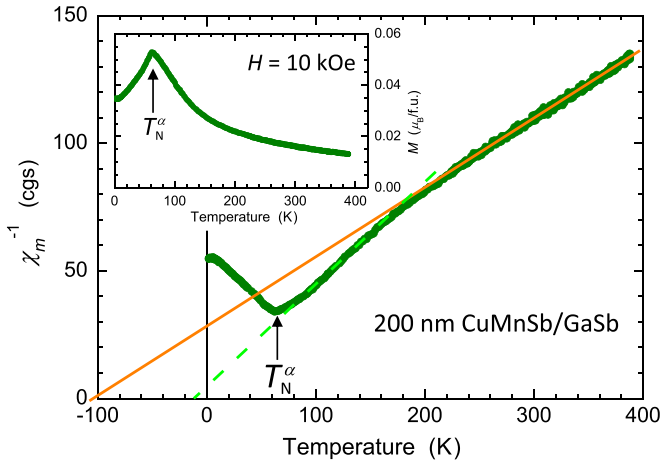

FIG. 4. Temperature T dependence of the inverse of the molar susceptibility, χ_m^{-1}, obtained for a 200-nm-thick CuMnSb film (green bullets). This dependence has been obtained from the temperature dependence of magnetization M in a bias field $H = 10$ kOe shown in the inset. The arrows indicate the position of the Néel temperature, $T_N^\alpha = 62$ K, on both plots. The solid orange and light green dashed lines indicate the Curie-Weiss behavior of $\chi_m^{-1}(T)$ for $T > 200$ K and for $T_N < T < 200$ K, respectively.

in the three stripe orientations, we obtain that the estimated volume fraction amounts to 0.7(4) percent.

The calculated properties of β–CuMnSb, such as its lattice parameters, stability, and magnetic properties, are discussed in detail in Sec. III C. Anticipating, we mention that they are consistent with experiment. We have also considered a second possible structure which is (almost) compatible with the TEM data, $Cu_3Mn_2Sb_2$, depicted in Fig. 2(c). However, this compound is higher in energy than the β phase, and was dropped from further considerations.

C. Magnetic properties

We begin with measurements of the magnetic properties at relatively high magnetic field of $H = 10$ kOe. They demonstrate that the dominant magnetic phase of our 200-nm-thick layer of CuMnSb is AFM, as expected. However, the temperature dependence of susceptibility also shows the presence of a second phase, which modifies the Curie-Weiss behavior at low temperatures. Detailed investigations performed at low and/or vanishing magnetic fields are presented in the second part of this section. They point out that the second phase is ferromagnetic.

The temperature T dependence of the magnetization, $M(T)$, obtained at $H = 10$ kOe is shown in the inset to Fig. 4. The clear kink on $M(T)$ at $T_N^\alpha = 62$ K marks the position of the paramagnetic to antiferromagnetic Néel transition. The superscript α denotes the fact that, as elaborated below, only the cubic α–CuMnSb part of the film undergoes the transition. This value corresponds exactly to the values of Néel point previously obtained for CuMnSb/GaSb films of the thickness $t \geqslant 200$ nm, which indirectly [29] indicates stoichiometric composition of this film.

More specific information about the magnetic state of the sample is obtained by examining the temperature dependence of the inverse magnetic susceptibility, $\chi^{-1}(T) = H/M(T)$, shown in the main panel of Fig. 4. The experimental $\chi^{-1}(T)$ at $T > T_N^\alpha$ can be approximated by two straight lines. The abscissa of the first one, which approximates $\chi^{-1}(T)$ above 200 K (the solid orange line in Fig. 4), yields exactly the same value of the Curie-Weiss temperature $T_{CW} = -100(5)$ K as that previously established for a thicker 510-nm layer, for which $\chi^{-1}(T)$ formed a single straight line above the Néel point under the same experimental conditions [29]. The slope of this line yields the value of the effective magnetic moment $\mu_{eff} = 5.4(1)\,\mu_B$/f.u., which is very close to the previously found value: $\mu_{eff} = 5.6\,\mu_B$/f.u. [29] This correspondence indicates that the high temperature part of $\chi^{-1}(T)$ is predominantly determined by AFM excitations in the paramagnetic matrix of CuMnSb and that at $H \geqslant 10$ kOe and $T \geqslant 200$ K no other contributions affect the magnetic signal. These basic magnetic properties obtained from the analysis described above are very close to those reported previously, as shown in Table I. The data from other studies show a certain distribution, which may indicate that other factors, such as a weak crystalline disorder, may be at work. In particular, either additional Mn interstitial ions or Cu_{Mn}-Mn_{Cu} antisite pairs are likely to form [35]. The presence of such defects was proposed to stabilize the experimentally observed AFM {111}-oriented phase of α–CuMnSb [35]. However, we do not observe a canted AFM order at low temperatures [41] in any of our samples.

We now turn to the significant change of the slope of $\chi^{-1}(T)$ at around 200 K. The abscissa of the second straight line, which approximates the experimental data between T_N^α and 200 K (marked as the dashed light green line in Fig. 4), yields a more positive value of the Curie-Weiss temperature, namely $T'_{CW} = -10(10)$ K. Interestingly, a somewhat stronger effect, characterized by a change of sign of T_{CW} to $T'_{CW} = +60(10)$ K, was noted in 40 nm CuMnSb layer grown on InAs [34]. We argue that this positive shift in T_{CW} can be taken as an indication of the existence of a FM component within the dominating AFM phase of the material. In accordance with the findings of structural characterization we propose that the dominating AFM component originates from the host α

TABLE I. Experimental Néel temperature T_N, effective Curie-Weiss magnetic moment of Mn ions m_{eff}(Mn), and Curie-Weiss temperature T_{CW} of α–CuMnSb. Measured orientation of the AFM axis is also given (n.e. = not established). References [42] and [41] report the saturation Mn moment.

T_N (K)	m_{eff}(Mn) (μ_B)	T_{CW} (K)	AFM order	Ref.
–	3.9(1)	–	[111]	[42]
55	3.95	−160(8)	[111]	[41]
55	5.4	−160	[111]	[43]
62	5.2	−120	n.e.	[44]
50	6.3	−250	n.e.	[45]
50	–	–	n.e.	[26]
62	5.9	−65	n.e.	[34]
62	5.6	−100	n.e.	[29]
62	5.5	−100	n.e.	This work

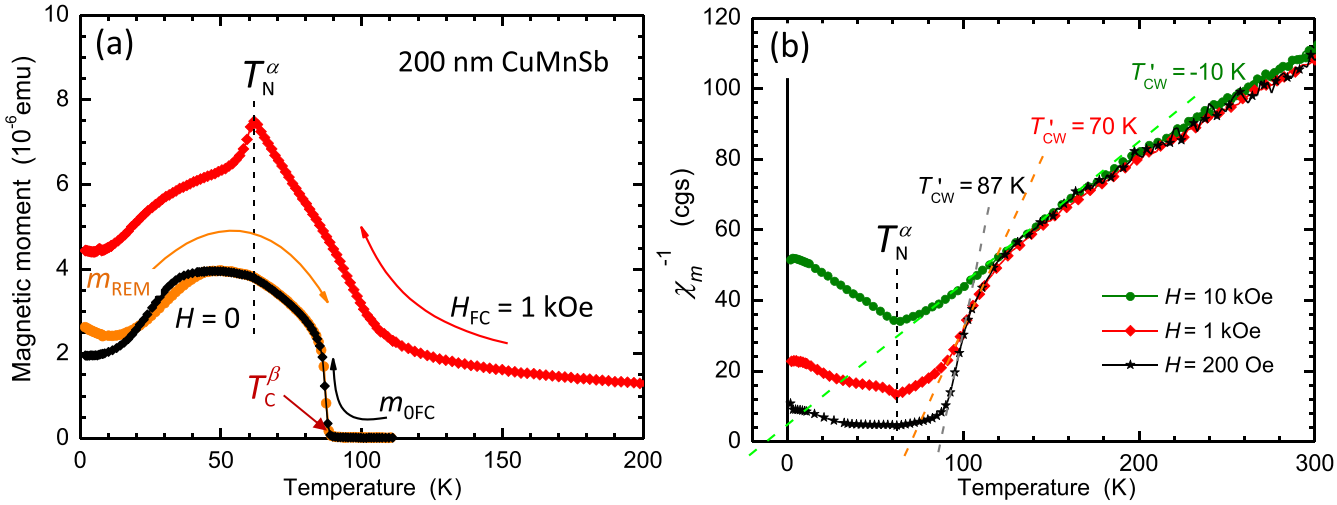

FIG. 5. (a) Temperature dependence of the magnetic moment in the weak magnetic field region. Red diamonds : field cooled sample in $H = 1$ kOe. The T dependence of the remnant magnetic moment m_{REM} during the warming (orange bullets), and during the cooling (black diamonds), $m_{0\mathrm{FC}}$, performed immediately after the m_{REM} measurement. Both warming and cooling measurements are performed under the same near zero field conditions ($H \simeq 0.1$ Oe). The Curie temperature of the FM component is $T_C^\beta \cong 88$ K. (b) Inverse susceptibility as a function of temperature measured in three magnetic fields, 10 kOe, 1 kOe, and 200 Oe. The graph illustrates the gradually increasing effect of the presence of the FM component in the sample on the magnitude of the apparent Curie-Weiss temperature, T'_{CW}, when the determination is made in a temperature range $90 < T < 200$ K, close to the Curie temperature T_C^β. The Néel temperature of the α–CuMnSb matrix, $T_N^\alpha = 62$ K, is shown in both panels.

phase, whereas the FM one is brought about by the embedded β–CuMnSb polymorph.

The main characteristics of the β–CuMnSb in the FM phase are obtained from the zero and near-zero magnetic field studies, where the magnetic response of the AFM α–CuMnSb is comparable or even smaller than that of the rapidly saturating FM part. In Fig. 5(a) we plot the magnitudes of the magnetic moment m recorded at remanence, m_{REM}. The sample is first cooled to the base temperature in $H = 1$ kOe (red diamonds), then the field is quenched, and the m_{REM} on warming is measured until the signal falls convincingly below the noise level. This main result is denoted by orange bullets, which give nonzero values that follow a Brillouin-like shape above 50 K, with a sharp cutoff at about 88 K. We take this point as an approximation of the Curie temperature T_C^β of the FM β–CuMnSb.

Technically, to perform the REM measurement the superconducting magnet of the SQUID magnetometer is carefully demagnetized to remove most of the trapped field left in the sample chamber after any previous high-field measurements. In addition, to further purify the system before the low T measurements we use the *magnet reset* option of our MPMS magnetometer to remove the $H = 1$ kOe field at which the sample is initially cooled. This option effectively soft-quenches the superconducting coil of the MPMS magnetometer. We independently estimate that our routine leaves about 0.1 Oe of the spurious field acting on the sample during the subsequent measurements.

Systems containing randomly dispersed magnetic precipitates (magnetic granules characterized by large macrospins) produce a superparamagnetic-like response. In particular, a nonzero m_{REM} is observed, signalizing the presence of energy barriers, which slow down macrospins' dynamics. However, in such a case the transition from $m_{\mathrm{REM}(T)} \neq 0$ to $m_{\mathrm{REM}(T)} = 0$ is considerably smeared out on the experimental timescale, and, more importantly, when the system is cooled back at $H = 0$ from above the temperature at which the m_{REM} vanishes, the experimental m remains zero down to the lowest T [39,46–49]. The results shown in Fig. 5(a) do not follow such a typical behavior. Indeed, right after the m_{REM} measurement is finished we cool back the sample from 110 K at the same zero field conditions. To distinguish between these two different measurements at remanence we denote the down-sweep in temperature, as in Ref. [39], $m_{0\mathrm{FC}}$ and denote it by black diamonds in Fig. 5(a). We find that $m_{0\mathrm{FC}}$ closely follows m_{REM} recorded on warming. $m_{0\mathrm{FC}}$ reproduces precisely even the very steep roll down of m_{REM} between 85 and 88 K. Remarkably, m rolls up equally swiftly on cooling. Undoubtedly, this is not the response one expects from an ensemble of randomly distributed macrospins [46]. Only coherently embedded ensembles of magnetically uniform nanocrystals (again: macrospins) or uniform ferromagnets with a strong uniaxial anisotropy ((Ga,Mn)As can be a good example here [47,50]) can exert a significant spontaneous magnetization on cooling through their Curie temperature. Therefore, such an $m_{0\mathrm{FC}}(T)$ indicates an orchestrated response of all of the β–CuMnSb inclusions present in the sample, confirming the pseudomorphic relationship between α and β polymorphs within CuMnSb established through the HRTEM characterization. Finally, the shapes of the low temperature parts of both m_{REM} and m_{FC0} indicate that below about 50 K the FM inclusions start to interact between themselves. This may originate in a partial AFM dipolar ordering between the macrospins. More detailed investigations of this feature go beyond the present work.

We now point out that it is this domelike FM contribution of the β–CuMnSb to the overall low field magnetization that

is responsible for both the change of slope of $\chi^{-1}(T)$, and the corresponding upshift of T_{CW} when established near T_C^{β}. We can already see this effect on the field-cooled data in Fig. 5(a), where the two bulges around 30 and 85 K reflect the unique shape of the T-dependent m of the FM component. It is noteworthy that the peak of $m(T)$ measured at 10 kOe (inset to Fig. 4) and 1 kOe [Fig. 5(a)], which marks the Néel transition, occurs at the same temperature, and there is no T_N^{α}-related feature seen on the $m(T)$ of the FM part. This absence of mutual coupling between both phases explains the lack of exchange bias like effects in our samples

The above-mentioned effect of the β–CuMnSb FM magnetization on the T-dependent properties of CuMnSb is illustrated in Fig. 5(b). We compare there $\chi^{-1}(T)$ taken at three values of $H = 0.2$, 1, and 10 kOe, finding that whereas above 200 K all three dependencies are identical within the experimental accuracy, below this temperature deviations from high-T linear relationship appear, which are the stronger the weaker is H applied during the measurement. We quantify this effect by establishing magnitudes of the apparent Curie-Weiss temperatures T'_{CW} from the second, semilinear part of $\chi^{-1}(T)$, as indicated by the corresponding dashed lines in Fig. 5(b). Clearly, the magnitudes of $T'_{CW} \to T_C \simeq 88$ K as $H \to 0$, indicating the domination of the β–CuMnSb FM response over the AFM one of the α–CuMnSb in weak magnetic fields. This substantial dependence on the bias field is the reason that, similarly to the study of the rock-salt AFM MnSb (Ref. [51]), we initially applied a rather strong bias field to infer the properties of the AFM part of the material.

The question arises whether the observed nonzero m_{REM} originates only from the β–CuMnSb inclusions, or from other (ferro)magnetic entities potentially present in the material, such as MnSb clusters. Indeed, compounds containing transition metals tend to precipitate magnetic nanocrystals [52]. However, this possibility can be definitively ruled out, because we do not detect any foreign crystalline forms during our HRTEM studies. Moreover, the measured value of the m_{REM} allows us to confidently estimate that the volume of the FM phase represents about 0.5(3) percent of the total volume of the system. This is consistent with the estimated relative volume of the β–CuMnSb inclusions, estimated in the previous section to be 0.7(4) percent.

III. THEORY

A. Theoretical methods

Calculations are performed within the density functional theory [53,54] in the generalized gradient approximation of the exchange-correlation potential proposed by Perdew, Burke and Ernzerhof [55]. To improve description of $3d$ electrons, the Hubbard-type $+U$ correction on Mn is added [56–58]. The parameter $U(\mathrm{Mn}) = 1$ eV reproduces the known formation energy of the intermetallic CuMn alloy and gives a reasonable value of the Mn cohesive energy. We use the pseudopotential method implemented in the QUANTUM ESPRESSO code [59], with the valence atomic configuration $4s^{1.5}p^0 3d^{9.5}$ for Cu, $3s^2p^6 4s^2 p^0 3d^5$ for Mn, and $5s^2p^3$ for Sb ions. The plane-waves kinetic energy cutoffs of 50 Ry for wave functions and 250 Ry for charge density are employed. Finally, geometry relaxations are performed with a 0.05 GPa convergence criterion for pressure. In defected crystals ionic positions are optimized until the forces acting on ions become smaller than 0.02 eV/Å.

The properties of defected α–CuMnSb are examined using cubic $2a \times 2a \times 2a$ supercells with 96 atoms (i.e., 32 f.u.), while magnetic order of ideal crystals are checked using the smallest possible supercells. Here a is the equilibrium lattice parameter. The k-space summations are performed with a $6 \times 6 \times 6$ k-point grid for the largest supercell, and correspondingly denser grids are used for smaller cells.

Magnetic interactions and magnetic order depend on several factors, such as the exchange spin splitting of the d(TM) shells, charge states of TM ions, concentration of free carriers and their spin polarization, and the density of states (DOS) at the Fermi energy E_F. These factors are interrelated, and are calculated self-consistently within *ab initio* approach.

Considering first the localized magnetic moments we note that spin polarization of Co, Ni, and Cu ions in XMnZ compounds practically vanishes, while that of the d(Mn) shell is substantial [16,17,31]. The robustness of the Mn magnetic moment results from the large, 3–5 eV, spin splitting of the $3d$(Mn) states. In fact, in XMnZ the d(Mn) spin-up channel is occupied, while most of the spin-down d(Mn) states lay above the Fermi level. Here, one can observe that spin polarization of the d(TM) electrons in free atoms depends on the difference in the number of spin-up and spin-down electrons, which is the highest in the case of Mn. Consequently, the Mn spin polarization persists in XMnZ. However, spin splitting of d electrons of Co and Ni atoms is smaller, and thus it vanishes in XMnSb hosts, see the analysis for TM dopants in ZnO [60].

In CuMnSb, the magnetic sublattice consists of Mn ions, which are second neighbors distant by 4.3 Å. Therefore, the direct exchange coupling between two Mn ions, given by overlaps of their d(Mn) orbitals, is negligibly small. The remaining indirect exchange coupling is the sum of two contributions, and the exchange constant $J_{\mathrm{indirect}} = J_{sr} + J_{RKKY}$ [16,17,61]. The first term J_{sr} has a short-range AFM character, and it is inversely proportional to the energy distance between the unoccupied d(Mn) states and E_F. The second coupling channel is of RKKY type mediated by free carriers. This channel depends on the detailed electronic structure in the vicinity of E_F, and J_{RKKY} is proportional to DOS(E_F). In particular, CoMnSb and NiMnSb half-metals are FM, while CuMnP and CuMnAs insulators are AFM. As we show here, CuMnSb is the border case.

B. Crystal and magnetic properties of α–CuMnSb

A rhombohedral primitive cell of α–CuMnSb contains one formula unit. This structure consist in four interpenetrating fcc sublattices, one of them being empty. The consecutive (001) MnSb planes are followed by the "half-empty" Cu planes, in which the planar atomic density is twice lower. The cubic unit cell is presented in Fig. 2(a). Local coordination of Mn ions can be relevant from the point of view of magnetic interactions. With this respect we notice that the magnetic coordination of an Mn ion consists in 12 equidistant Mn atoms at $a/\sqrt{2}$. Moreover, the short-range coupling between two Mn nearest neighbors is mediated through the closest ions, and it

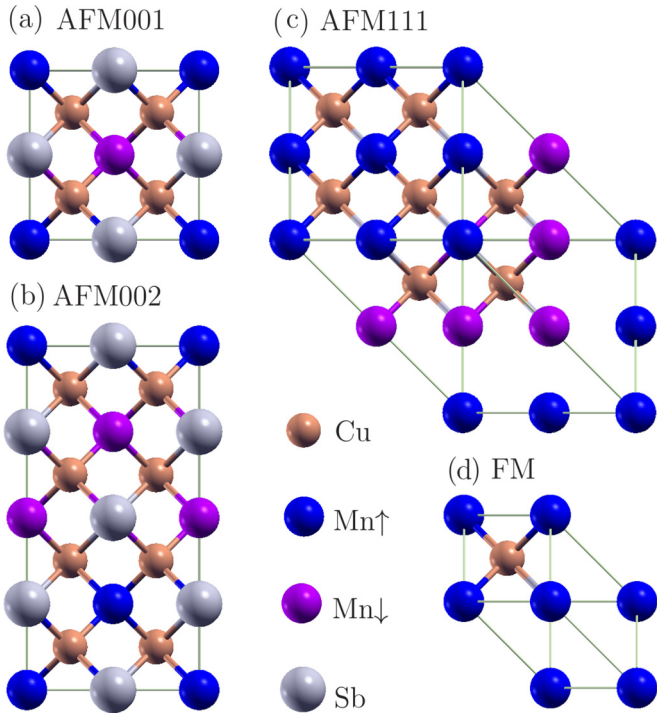

FIG. 6. Side view of the considered magnetic cells: (a) antiferromagnetic with {001} planes with the same Mn spins shown in the $a \times a \times a$ cell (AFM001), (b) antiferromagnetic with double {001} planes of the same spins on Mn ions in the $a \times a \times 2a$ cell (AFM002), (c) antiferromagnetic with ferromagnetic {111} planes realized in the $a\sqrt{2} \times a\sqrt{2} \times a\sqrt{2}$ cell (AFM111), and (d) ferromagnetic in primitive rhombohedral cell $a/\sqrt{2} \times a/\sqrt{2} \times a/\sqrt{2}$ (FM). Mn atoms with different spin directions are indicated as Mn ↑ and Mn ↓.

occurs through one Mn-Cu-Mn "bridge" and two Mn-Sb-Mn "bridges."

We consider four magnetic phases of α–CuMnSb. The corresponding supercells are shown in Fig. 6. Antiferromagnetic order with parallel Mn spins in the (001) planes, AFM001, is calculated using the cubic $a \times a \times a$ cell with 4 f.u. (12 atoms), and shown in Fig. 6(a). The AFM order with a period doubled in the [001] direction with parallel Mn spins in each (001) plane, denoted as AFM002, is shown in Fig. 6(b). The corresponding $a \times a \times 2a$ cell contains 8 f.u., and is one of the possible supercells in which this phase can be realized. In the AFM111 phase, the Mn spins are parallel in each (111) plane, but the consecutive (111) planes are AFM, as shown in Fig. 6(c), and the corresponding rhombohedral unit cell $a\sqrt{2} \times a\sqrt{2} \times a\sqrt{2}$ contains 8 primitive cells with 24 atoms. Finally, the FM phase requires a primitive cell $a/\sqrt{2} \times a/\sqrt{2} \times a/\sqrt{2}$ with 1 f.u., presented in Fig. 6(d).

The obtained results are collected in Table II and in Fig. 7. The ground state structure is AFM001, but the experimentally observed AFM111 is only 7 meV per f.u. higher in energy. The least stable is the FM order, higher in energy than AFM001 by about 20 meV per f.u. The equilibrium lattice parameters $a \approx 6.1$ Å are practically independent of the magnetic order, and close to the experimental value 6.088 Å [42]. Some phases are characterized by a small distortion

TABLE II. The calculated lattice parameter a, the saturation Mn magnetic moment, m_{sat}, and the energy of the given magnetic order relative to α–CuMnSb in the AFM001 ground state, ΔE_{tot}. All energies are per one formula unit. Our measured TEM values are also given.

	a (Å)	c (Å)	$m_{\text{sat}}(\mu_B)$	ΔE_{tot} (meV)
α–CuMnSb				
AFM001	6.10	–	4.59	0
AFM002	6.09	–	4.61	3
AFM111	6.10	–	4.55	7
FM	6.11	–	4.70	19
TEM	6.2(1)	–	–	–
β–CuMnSb				
AFM	5.83	6.40	4.48	113
FM	5.88	6.28	4.52	102
TEM	5.8(1)	6.2(1)	–	–

of the cubic symmetry caused by different bond lengths between ferromagnetically and antiferromagnetically oriented Mn ions. Differences in the lattice parameters between various magnetic phases are below 0.01 Å, and are not reported in the Table. Similar results for the AFM001 order were obtained in Ref. [35], while in Refs. [16,31] the AFM order is more stable than FM by 50 and 90 meV per Mn, respectively.

The last property reported in Table II is the saturation magnetic moment of Mn, which also is similar in all phases, and equal to about $4.6\,\mu_B$. This value corresponds to the Curie-Weiss moment of $5.5(1)\,\mu_B$, and compares favorably with the experimental values given in Table I.

The obtained results allow estimating the relative roles of the short- and long-range contributions to the magnetic coupling. To this end, we assume the hamiltonian in the form $H_{ex} = -J/2 \sum_{i,j} \vec{s}_i \vec{s}_j$, where the short-range interaction is limited to the Mn NNs neighbors, and the long-range term is neglected. The spin value, $s_i \approx 2.3$, is one half of the calculated magnetic moment of Mn.

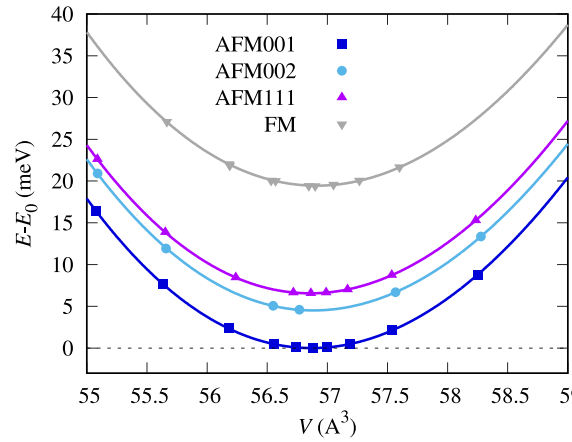

FIG. 7. Volume dependence of the total energy relative to the ground state $E_0 = E_{\text{AFM001}}(V_0)$ of α–CuMnSb in the AFM001, AFM002, AFM111 and FM phases. Both volume and energy are per formula unit. Lines are fitted to the calculated values (symbols).

The exchange constant J is positive (negative) for the FM (AFM) coupling, and is obtained by comparing energies of various magnetic orders. In the AFM001 phase, each Mn ion has four ferromagnetically oriented Mn NNs in the (001) plane and eight antiferromagnetically oriented Mn NNs in the two adjacent planes. For the remaining magnetic phases, the energies calculated relative to the ground state $E_0 \equiv E_{\mathrm{AFM001}}$ depend on the magnetic order as shown in Table II. These results give the coupling constant in the range $-0.6 \geqslant J_{\mathrm{sr}} \geqslant -0.2$ meV. This spread is quite large and cannot be explained by (negligible) changes in atomic distances in cells with different magnetic ordering. Therefore, we conclude that the Heisenberg nearest-neighbor model does not describe magnetic properties of *bulk* phases. Indeed, such a model is not appropriate for metallic or semimetallic systems such as α–CuMnSb, where the long-range RKKY coupling is present.

An opposite conclusion comes from the analysis of *single spin* excitations from the AFM001 ground state. We use a $2a \times 2a \times 2a$ supercell to calculate the energy differences ΔE for the following cases, in which we change (i) spin of one Mn ion, $1\mathrm{Mn}\uparrow \rightarrow 1\mathrm{Mn}\downarrow$, called a single spin-flip, (ii) $2\mathrm{Mn}\uparrow \rightarrow 2\mathrm{Mn}\downarrow$ for spins of two nearest Mn ions belonging to one layer, and (iii) $2\mathrm{Mn}\uparrow \rightarrow 2\mathrm{Mn}\downarrow$ for two distant Mn ions. In these processes the long-range coupling is not important, and indeed the calculated exchange constant consistently is $J_{\mathrm{sr}} \approx -0.4$ meV.

C. Crystal and magnetic properties of β–CuMnSb

We now consider two possible structures of the secondary phase proposed based on the experimental results. They are characterized by doubling the periodicity in the [001] direction. The unit cell of β–CuMnSb, shown in Fig. 2, is tetragonally deformed relative to that of α–CuMnSb, with the corresponding lattice parameters $a = 5.88$ Å and $c = 6.275$ Å. They differ by about 3 percent from our calculated cubic $a(\alpha - \mathrm{CuMnSb}) = 6.105$ Å. The two interlayer spacings between the consecutive MnSb planes in the [001] direction in the unit cell, shown in Fig. 2(b), are quite different, namely $d_{\mathrm{inter1}} = 2.80$ Å (no Cu), and $d_{\mathrm{inter2}} = 3.48$ Å (with Cu). Turing to the magnetic order of β–CuMnSb, we find that the FM phase constitutes the ground state with $m_{\mathrm{sat}} = 4.6\,\mu_{\mathrm{B}}$ and is lower than the AFM phase by 11 meV per f.u., as indicated in Table II. Thus, the two crystalline phases of CuMnSb are in two different magnetic phases.

The experimental [27] lattice parameters of β–CuMnSb reasonably agree with our values, i.e., the calculated $a = 6.28$ Å and $c/a = 1.87$ are about 2% larger than those measured for the *compressed* crystal at the critical pressure of 7 GPa. However, the calculations of Ref. [27] predict that the magnetic order of the β phase is AFM, in striking contrast with our results. Also their calculated $m_{\mathrm{sat}}(Mn) = 3.8\,\mu_{\mathrm{B}}$ is substantially smaller than our $4.6\,\mu_{\mathrm{B}}$. The origin of these discrepancies is not clear, but it may be due to the different exchange-correlation functionals used, and/or to application of the $+U(\mathrm{Mn})$ correction in our calculations (which can affect the results [31]).

The calculated total energy of the FM β–CuMnSb relative to the AFM α–CuMnSb is higher by 102 meV per f.u. This energy difference is not large, being comparable to the growth temperature, which implies that the β–CuMnSb polymorph can indeed form during epitaxy. We also stress that stoichiometry of the α and β phases is the same, which facilitates formation of β–CuMnSb. Finally, the observed β–CuMnSb inclusions are coherent, i.e., lattice matched, with the host structure. This agrees with the fact that the calculated excess elastic energy of matching the lattice parameters of the β phase to the host α phase is very low and ranges from 3 meV per f.u. (when the tetragonal a parameter constrained to the cubic $a = 6.105$ Å) to 20 meV per f.u. (the tetragonal c parameter constrained to the cubic a).

The second considered possibility, $Cu_3Mn_2Sb_2$ shown in Fig. 2(c), is higher in energy by 0.37 eV per f.u. in the Cu–rich conditions than the ideal CuMnSb, i.e., by 0.27 eV per f.u. than β–CuMnSb, its stoichiometry is markedly different, and thus we can eliminate this structure from considerations.

D. Energy band structures of α–CuMnSb and β–CuMnSb

Figure 8(a) shows the energy bands and DOS of the AFM001 α–CuMnSb. We see that this phase has a metallic character, however DOS at the Fermi level is low. The states close to E_{F} are built from s, p and d states of all ions with similar weights. The low $\mathrm{DOS}(E_{\mathrm{F}})$ makes CuMnSb almost semimetallic with a low electrical conductivity. Compatible with the small $\mathrm{DOS}(E_{\mathrm{F}})$ is the high resistivity measured in Refs. [41,62].

Since the system is antiferromagnetically ordered, the total DOSs of spin-up and spin-down states are the same. In Fig. 8 only contributions of the $3d(\mathrm{Mn})$ and $3d(\mathrm{Cu})$ orbitals are presented to reveal magnetic properties. We see that the exchange spin splitting of the $d(\mathrm{Mn})$ shell is large, about 5 eV. The closely spaced levels contributing to the DOS maxima centered at 4 eV below the Fermi energy are composed mainly of the d states of both Cu and Mn. Spin-up and spin-down $3d(\mathrm{Cu})$ orbitals are almost completely occupied, and thus Cu ions are nonmagnetic. In turn, the majority spin states of the $3d(\mathrm{Mn})$ orbitals are completely occupied, while the minority spin states at 1 eV above the Fermi energy are partially filled thanks to a small overlap with spin-up states. As a result, a single Mn ion is in between the d^5 and d^6 configuration, with the saturation magnetic moment of $4.6\,\mu_{\mathrm{B}}$ consistent with Table II. Our results for α–CuMnSb are close to those of Ref. [31]. A similar electronic configuration takes place in CuMnAs, where the spin-down Mn states are partially filled [63].

The overall band structure of the FM β–CuMnSb displayed in Fig. 8(b) is close to that of α–CuMnSb, which is particularly clear when comparing partial DOS of both phases. In particular, $m_{\mathrm{sat}}(\mathrm{Mn})$ is about $4.5\,\mu_{\mathrm{B}}$ in both phases, and energies of both $d(\mathrm{Mn})$- and $d(\mathrm{Cu})$-related bands are largely independent of the actual crystal structure. This similarity can be due to the fact that the MnSb (001) planes play a dominant role, and the exact locations of the Cu ions are less important.

However, the calculated $\mathrm{DOS}(E_{\mathrm{F}})$ for the α phase is 0.35 states per spin and f.u., while for the β phase we find 1.26 states per spin and f.u., which is 3.6 times higher. As a consequence, α–CuMnSb is semimetallic, and the AFM order is dominant, while β phase is more metallic in character, which in turn favors the RKKY-type coupling and the FM order. This

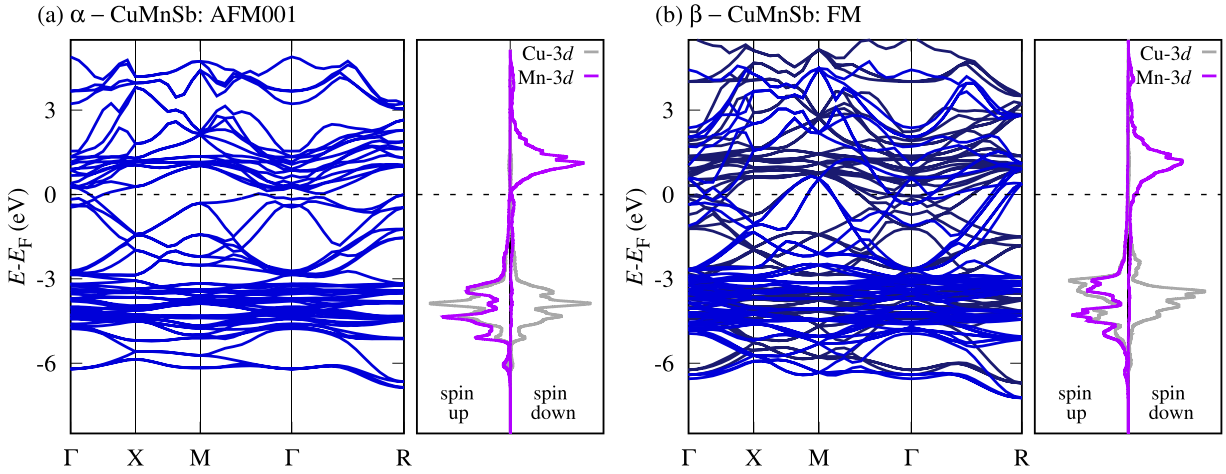

FIG. 8. Bands and partial DOSs for (a) the AFM001 of α–CuMnSb and for (b) the FM state of β–CuMnSb obtained using the $a \times a \times c$ cell. The right panels show the partial DOSs for Cu and Mn ions, and thus different contributions to spin-up and spin-down density of Mn $\uparrow$ are exposed also in AFM case. In panel (b) the spin degeneracy is lifted.

feature can explain the different magnetic phases of the α and β polymorphs.

Analysis of the calculated electronic structure of Heusler and half-Heusler CuMnZ led Sasioglu *et al.* [17] to the conclusion that when the spin polarization of conduction electrons is large, and the d(Mn) spin-down states are far above E_F, then the RKKY coupling is dominant, and one should expect the FM order, otherwise the short-range AFM coupling is dominant. Our results do not confirm this conclusion, and indicate that the important factor determining the magnetic order is the DOS(E_F).

E. Point native defects in α–CuMnSb

Formation energy of a defect D is given by

$$E_{\text{form}}(\text{D}) = E(\text{CuMnSb}:\text{D}) - E(\text{CuMnSb}) + \sum_i n_i \mu_i, \quad (1)$$

where E(CuMnSb) and E(CuMnSb : D) are the total energies of a supercell without and with a defect, and $n_i = +1(-1)$ corresponds to the removal (addition) of one ith atom. μ_is are the variable chemical potentials of atoms in the solid, which in general are different from the chemical potentials μ_i(bulk) of the standard state of elements, i.e., Cu, Mn, and Sb bulk. Details of calculations of chemical potentials are given in the Appendix.

The point native defects considered here are vacancies V_X, interstitials X_i, and antisites X_Y (where X and Y are Cu, Mn, or Sb) for all three sublattices. As it was mentioned above, the Cu sublattice is "half- empty" compared to the MnSb sublattice. Consequently, we consider here formation of interstitials at the empty sites of the Cu sublattice only, and neglect other possibilities, expected to have higher formation energies E_{form}. Thus, the set of defects considered here only partially overlaps with that of Ref. [35]. Of particular interest to the present study are defects involving Mn ions, since they can influence magnetic properties of α–CuMnSb [35]. This is why we consider them more extensively, after briefly analyzing the nonmagnetic defects. The calculated formation energies are summarized in Table III. Because of the magnetic coupling, formation energies of the Mn-related defects depend on the spin direction relative to the spins of the host Mn neighbors. We consider possible spin configurations shown in Fig. 9(b).

Formation energy determines the corresponding equilibrium concentration $[D]$ of a defect D according to

$$[D] = N_0 \exp[-E_{\text{form}}(D)/k_B T], \quad (2)$$

where k_B is the Boltzmann constant and N_0 is the density of the relevant lattice sites. Details of the calculations of E_{form} are provided in the Appendix. To put the calculated formation energies into a proper context, we note that if the growth temperature $T_{\text{growth}} = 250^\circ$C and $E_{\text{form}} = 0.1$ eV, then $\exp(-E_{\text{form}}/k_B T_{\text{growth}}) = 0.1$, which corresponds to a high 10 atomic percent concentration of this defect on the considered sublattice. However, if $E_{\text{form}} = 1$ eV, then $\exp(-E_{\text{form}}/k_B T_{\text{growth}}) = 9 \times 10^{-11}$, which implies a negligible defect concentration.

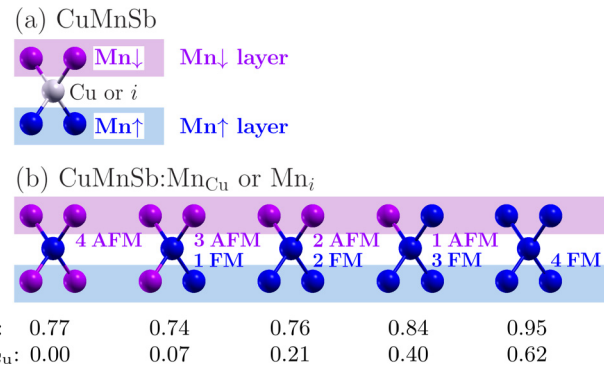

FIG. 9. All possible spin orientations of Mn ions in α–CuMnSb AFM001. In the ground state configuration, the Mn spins are parallel within each MnSb (001) layer, and the consecutive MnSb (001) layers are AFM, as shown in panel (a). (b) Mn Mn_{Cu} antisites and Mn_i interstitials can assume 5 different local spin configurations. The corresponding spin-dependent formation energies in eV are given by the numbers below.

TABLE III. Formation energies (in eV) of isolated point defects in the Mn-rich conditions. In parentheses are Mn-related values corrected for $\Delta H_f(\mathrm{MnSb}) = 0.48$ eV, which correspond to the Mn-poor case.

Cu defects		Sb defects		Mn defects	
V_{Cu}	−0.01	V_{Sb}	2.45	V_{Mn}	−0.07 (−0.55)
Cu_i	1.00	Sb_i	3.64	Mn_i	0.74–0.95 (1.22–1.43)
Cu_{Mn}	0.48 (0.00)	Sb_{Mn}	1.60 (1.12)	Mn_{Cu}	0.00–0.62 (0.48–1.10)
Cu_{Sb}	1.20	Sb_{Cu}	2.82	Mn_{Sb}	1.18 (1.65)

1. Sb sublattice

The prohibitively high values of E_{form} demonstrate that V_{Sb} and Sb_i should not form. Similarly, formation energies of Sb_{Cu}, Sb_{Mn}, Cu_{Sb}, and Mn_{Sb} antisites exceed 1 eV, and those defects are not expected to be present at high concentrations. Consequently, the Sb sublattice is thermodynamically stable, robust, and constitutes a defect-free back-bone of CuMnSb.

2. Cu and Mn sublattices

The properties of both Cu and Mn sublattices are opposite to those of the Sb sublattice, as they are susceptible to contain defects. In particular:

(i) Both the Cu and Mn vacancies can be present at high concentrations, since their E_{form} are low.

(ii) Formation energy of Cu interstitials at the Cu sublattice, $E_{\mathrm{form}}(\mathrm{Cu}_i) = 1$ eV, is relatively high, and their concentrations are negligible. Additionally, the high formation energy of Cu_i interstitials is consistent with the sparse character of the Cu sublattice in α–CuMnSb.

(iii) Formation of Mn_i interstitials at the Cu sublattice is characterized by $E_{\mathrm{form}} = 0.7$-1.4 eV, depending on the spin direction and conditions of growth, and therefore they are not expected to be present at high concentrations, especially in the Mn-poor conditions.

(iv) Finally, Mn_{Cu} antisites, with formation energies ranging from 0 to about 1 eV, can be present at high concentrations, comparable to those of V_{Mn} and V_{Cu}.

In brief, low formation energies are found for three defects, namely the V_{Cu} and V_{Mn} vacancies and the Mn_{Cu} antisite, particularly at the Mn-rich growth conditions. This indicates that a Cu deficit on the Cu sublattice is possible, affecting stoichiometry. Significantly, Mn_{Cu} antisites make the Cu sublattice magnetic, and also they can participate in the magnetic coupling between the adjacent MnSb (001) planes, thus influencing magnetic properties, as it will be discussed in more detail below. In contrast, Sb_{Cu} antisites are present in negligible concentrations. Our results are in a reasonable agreement with those of Ref. [35], especially given their neglect of spin effects and a somewhat different theoretical approach. Interestingly, formation energies of native defects in CuMnAs calculated in Ref. [63] are close to the present results in spite of the different anion.

F. Defect-induced magnetic coupling

There are two Mn-related point defects, Mn_i and Mn_{Cu}, both situated on the Cu sublattice. When present at high concentrations, they affect magnetism of α–CuMnSb. Their coupling with host Mn ions is different than the Mn-Mn coupling between the host Mn because of the different local coordination. Energetics of both defects is complex and rich, since the total energy of the system (and thus formation energies) depends on their spin orientations relative to the neighborhood. At both substitutional and interstitial sites in the Cu layer, a Mn ion has 4 Mn nearest neighbors arranged in a tetrahedral configuration, 2 in the upper and 2 in the lower MnSb layer. The Mn_i–Mn_{Mn} distance is shorter than that of Mn_{Mn}–Mn_{Mn}, and equal to $(\sqrt{3}/4)a$.

The possible local spin configurations are reduced to small clusters of 5 Mn ions, shown in Fig. 9. The Mn spin-up and spin-down (001) MnSb layers are denoted by in pink and blue, respectively, reflecting the calculated (001) AFM magnetic ground state. The central Mn_{Cu} (or Mn_i) ion of such a cluster provides an additional channel of magnetic coupling between two adjacent MnSb layers. The corresponding formation energies are given in Fig. 9.

As it was pointed out, in ideal α–CuMnSb, the Mn ions are second neighbors only, separated either by Sb [i.e., the Mn-Sb-Mn "bridge" in the MnSb(001) plane] or by Cu [forming a Mn-Cu-Mn "bridge" linking 3 consecutive (001) planes]. Thus, the short-range magnetic coupling in ideal α–CuMnSb is successfully modelled in Sec. III B by the interaction between two Mn *second neighbors*, situated either in the same MnSb layer, or in two adjacent ones. In contrast, the four host Mn ions in the cluster are the *first* neighbors of a Mn_i or a Mn_{Cu} defect. Thus, one can expect that this coupling is stronger than the intrinsic one in the ideal host, and indeed, the differences in energy between various configurations in Fig. 9 are about 100 meV, which is too high to be explained by the estimated $J_{\mathrm{sr}} = 0.4$ meV.

As it follows from Fig. 9, 5-atom clusters are magnetically frustrated. In particular, the lowest energy case denoted as 4AFM favors the local FM orientation of spins in two adjacent (001) planes, which is opposite to the global host magnetic order. Our results do not confirm the conclusion of Ref. [63] who find that the 3AFM configuration has the lowest energy, and thus it promotes the global AFM111 order. Instead, we rather expect that Mn-related point defects induce disorder of the host AFM phase, possibly leading to formation of a spin glass [64].

IV. SUMMARY

CuMnSb films were epitaxially grown on GaSb substrates. Magnetic measurements reveal the presence of two magnetic subsystems. The dominant magnetic order is AFM with the Néel temperature of 62 K, which is the same as in bulk CuMnSb. It coexists with a FM phase, characterized by the Curie temperature of about 100 K.

These findings go in hand with transmission electron microscopy and selective area diffraction measurements, which demonstrate coexistence of two structural polymorphs of the same stoichiometry. The dominant one is the cubic half-Heusler α–CuMnSb, which is the equilibrium structure of bulk samples. The second component is a tetragonal β–CuMnSb polymorph, which forms 10–100 nm long elongated inclusions.

The results of our *ab initio* calculations provide a consistent interpretation of the experimental data and, in particular:

(i) The β–CuMnSb phase is metastable, and its total energy is higher by 0.1 eV per f.u. only than that of the equilibrium α–CuMnSb. Lattice parameters of the β phase differ from those of α–CuMnSb by about 4 percent. This lattice misfit between the two structures does not prevent the pseudomorphic coexistence of both phases, since the calculated misfit strain energy is below 20 meV per f.u.

(ii) In agreement with experiment, α–CuMnSb is AFM, and the FM order is 19 meV per f.u. higher in energy. In contrast, the magnetic ground state of β–CuMnSb is FM, which is more stable than AFM by 11 meV per f.u. This indicates that indeed the β–CuMnSb inclusions are responsible for the FM signal.

(iii) The different magnetic orders of the α and β phases originate in their somewhat different band structures. In particular, critical for magnetic order is the DOS at the Fermi level, which is about four times higher in β–CuMnSb than in the α phase. This shows that the β phase is more metallic in character, which in turn favors the FM order driven by the Ruderman-Kittel-Kasuya-Yoshida interaction.

(iv) Our calculations predict the saturated magnetic moment of Mn $m_{\mathrm{sat}} = 4.6\,\mu_{\mathrm{B}}$ and $4.5\,\mu_{\mathrm{B}}$ for the α and the β phase, respectively. This corresponds to the effective moment of $5.6\,\mu_{\mathrm{B}}$, in good agreement with the measured $5.5\,\mu_{\mathrm{B}}$.

(v) The calculated formation energies of point native defects indicate that the most probable are the $\mathrm{Mn_{Cu}}$ antisites with low formation energies of 0–0.2 eV. However, their presence is expected to disorder the host magnetic AFM phase rather than to induce a transition to the FM configuration.

(vi) Regarding the properties of the CuMnX series we see that their structural stability is relatively weak, as they crystallize in a variety of structures. In particular, unlike the bulk orthorhombic CuMnAs, epitaxial films of CuMnAs are tetragonal, but both structures are AFM. In the case of CuMnSb, polymorphism comprises also the equilibrium magnetic structure, AFM in the bulk specimens, and FM in epitaxial films.

ACKNOWLEDGMENTS

L.S., C.G., J.K., and L.W.M. thank M. Zipf for technical assistance. Our work was funded by the Deutsche Forschungsgemeinschaft (DFG, German Research Foundation), Grant No. 397861849, by the Free State of Bavaria (Institute for Topological Insulators), and by the Deutsche Forschungsgemeinschaft (DFG, German Research Foundation) under Germany's Excellence Strategy Grant No. EXC2147 ct.qmat (Project ID No. 390858490).

APPENDIX

The difference between chemical potential μ_i considered in formation energy, Eq. (1), and the chemical potential of bulk Cu, Mn, or Sb, $\mu_i(\mathrm{bulk})$, is denoted by $\delta\mu_i$:

$$\mu_i = \mu_i(\mathrm{bulk}) + \delta\mu_i. \tag{A1}$$

The highest possible value of μ_i is $\mu_i(\mathrm{bulk})$, which implies that the studied system is in equilibrium with the given bulk source of atoms and $\delta\mu_i = 0$; otherwise, $\delta\mu_i < 0$.

Chemical potentials of the components in the standard state are given by the total energies per atom of elemental solids. The calculated cohesive energies E_{coh} of the face centered cubic Cu, the face centered cubic Mn with the AFM magnetic order, and the triclinic Sb are, respectively, 3.40 (3.49), 2.65 (2.92), and 2.68 (2.75) eV/atom. They compare reasonably well with the experimental values given in parentheses [65].

Chemical potentials of the involved atomic species depend on possible formation of compounds. The ranges of variations of chemical potentials are determined by conditions of equilibrium between various phases, i.e., $\mathrm{Cu_2Sb}$, MnSb, and CuMnSb. Thermodynamic equilibrium requires that

$$\begin{aligned}
\delta\mu(\mathrm{Cu}) + 2\delta\mu(\mathrm{Sb}) &= \Delta H_f(\mathrm{Cu_2Sb}),\\
\delta\mu(\mathrm{Mn}) + \delta\mu(\mathrm{Sb}) &= \Delta H_f(\mathrm{MnSb}),\\
\delta\mu(\mathrm{Cu}) + \delta\mu(\mathrm{Mn}) + \delta\mu(\mathrm{Sb}) &= \Delta H_f(\mathrm{CuMnSb}),
\end{aligned} \tag{A2}$$

where ΔH_f is the enthalpy of formation per formula unit (negative for a stable compound).

The calculated values $\Delta H_f(\mathrm{Cu_2Sb}) = -0.03$ eV per f.u., $\Delta H_f(\mathrm{MnSb}) = -0.48$ eV per f.u., and $\Delta H_f(\mathrm{CuMnSb}) = -0.42$ eV per f.u. The very low $\Delta H_f(\mathrm{Cu_2Sb})$ is somewhat unexpected, since $\mathrm{Cu_2Sb}$ is a stable compound which crystallizes in the tetragonal phase [43]. Next, our result $\Delta H_f(\mathrm{MnSb}) = -0.48$ eV per f.u. agrees well with both the previous value -0.52 eV per f.u. calculated in Ref. [66], and the experimental -0.52 eV per f.u. [67]. Assuming that the accuracy of the calculated values is 0.03 eV per f.u., the set of Eq. (A2) is consistent if we assume $\Delta H_f(\mathrm{Cu_2Sb}) = 0$ and $\Delta H_f(\mathrm{MnSb}) = \Delta H_f(\mathrm{CuMnSb}) = -0.45$ eV per f.u. This in turn implies that $\delta\mu(\mathrm{Cu}) = \delta\mu(\mathrm{Sb}) = 0$ and $\delta\mu(\mathrm{Mn}) = -0.45$ eV. Consequently, the allowed window of the Mn chemical potential is

$$-0.45\,\mathrm{eV} < \delta\mu(\mathrm{Mn}) < 0, \tag{A3}$$

where the two limiting values correspond to the Mn-poor and Mn-rich conditions, and an analogous window holds for Sb.

[1] W. H. Meiklejohn and C. P. Bean, New magnetic anisotropy, Phys. Rev. **105**, 904 (1957).

[2] J Nogues and I. K. Schuller, Exchange bias, J. Magn. Magn. Mater. **192**, 203 (1999).

[3] D. Xiong, Y. Jiang, K. Shi, A. Du, Y. Yao, Z. Guo, D. Zhu, K. Cao, S. Peng, W. Cai, D. Zhu, and W. Zhao, Antiferromagnetic spintronics: An overview and outlook, Fund. Res. **2**, 522 (2022).

[4] W. A. Borders, A. Z. Pervaiz, S. Fukami, K. Y. Camsari, H. Ohno, and S. Datta, Integer factorization using stochastic magnetic tunnel junctions, Nature (London) **573**, 390 (2019).

[5] L. Wollmann, A. K. Nayak, S. S. P. Parkin, and C. Felser, Heusler 4.0: Tunable materials, Annu. Rev. Mater. Res. **47**, 247 (2017).

[6] J. E. Douglas, E. E. Levin, T. M. Pollock, J. C. Castillo, P. Adler, C. Felser, S. Krämer, K. L. Page, and R. Seshadri, Magnetic hardening and antiferromagnetic/ferromagnetic phase coexistence in $Mn_{1-x}Fe_xRu_{2-x}Sn$ Heusler solid solutions, Phys. Rev. B **94**, 094412 (2016).

[7] E. Decolvenaere, E. Levin, R. Seshadri, and A. Van der Ven, Modeling magnetic evolution and exchange hardening in disordered magnets: The example of $Mn_{1-x}Fe_xRu_2Sn$ Heusler alloys, Phys. Rev. Mater. **3**, 104411 (2019).

[8] E. McCalla, E. E. Levin, J. E. Douglas, J. G. Barker, M. Frontzek, W. Tian, R. M. Fernandes, R. Seshadri, and C. Leighton, Understanding magnetic phase coexistence in $Ru_2Mn_{1-x}Fe_xSn$ Heusler alloys: A neutron scattering, thermodynamic, and phenomenological analysis, Phys. Rev. Mater. **5**, 064417 (2021).

[9] D. Y. Cong, S. Roth, M. Pötschke, C. Hürrich, and L. Schultz, Phase diagram and composition optimization for magnetic shape memory effect in Ni, Co, Mn, Sn alloys, Appl. Phys. Lett. **97**, 021908 (2010).

[10] S. Yuan, P. L. Kuhns, A. P. Reyes, J. S. Brooks, M. J. R. Hoch, V. Srivastava, R. D. James, and C. Leighton, Phase separation and superparamagnetism in the martensitic phase of $Ni_{50-x}Co_xMn_{40}Sn_{10}$, Phys. Rev. B **93**, 094425 (2016).

[11] M. Halder, S. M. Yusuf, A. Kumar, A. K. Nigam, and L. Keller, Crossover from antiferromagnetic to ferromagnetic ordering in the semi-Heusler alloys $Cu_{1-x}Ni_xMnSb$ with increasing Ni concentration, Phys. Rev. B **84**, 094435 (2011).

[12] S. K. Ren, W. Q. Zou, J. Gao, X. L. Jiang, F. M. Zhang, and Y. W. Du, Magnetic behavior of half-Heusler alloy $Cu_xNi_{1-x}MnSb$, J. Magn. Magn. Mater. **288**, 276 (2005).

[13] S. K. Ren, Y. X. Wang, Y. J. Zhang, G. B. Ji, F. M. Zhang, and Y. W. Du, Magnetic and electrical properties of the half-Heusler $Cu_xNi_{1-x}MnSb$ alloys, J. Alloys Compd. **387**, 32 (2005).

[14] N. P. Duong, L. T. Hung, T. D. Hien, N. P. Thuy, N. T. Trung, and E. Brück, Magnetic properties of half-metallic semi Heusler $Co_{1-x}Cu_xMnSb$ compounds, J. Magn. Magn. Mater. **311**, 605 (2007).

[15] K. Endo, Magnetic Studies of Clb-Compounds CuMnSb, PdMnSb and Cu_{1-x}(Ni or Pd)$_x$MnSb, J. Phys. Soc. Jpn. **29**, 643 (1970).

[16] I. Galanakis, E. Şaşıoğlu, and K. Özdoğan, Magnetic phase transition in half-metallic CoMnSb and NiMnSb semi-Heusler alloys upon Cu doping: First-principles calculations, Phys. Rev. B **77**, 214417 (2008).

[17] E. Şaşıoğlu, L. M. Sandratskii, and P. Bruno, Role of conduction electrons in mediating exchange interactions in Mn-based Heusler alloys, Phys. Rev. B **77**, 064417 (2008).

[18] T. Jungwirth, J. Sinova, A. Manchon, X. Marti, J. Wunderlich, and C. Felser, The multiple directions of antiferromagnetic spintronics, Nat. Phys. **14**, 200 (2018).

[19] P. Wadley, V. Hills, M. R. Shahedkhah, K. W. Edmonds, R. P. Campion, V. Novak, B. Ouladdiaf, D. Khalyavin, S. Langridge, V. Saidl, P. Nemec, A. W. Rushforth, B. L. Gallagher, S. S. Dhesi, F. Maccherozzi, J. Zelezny, and T. Jungwirth, Antiferromagnetic structure in tetragonal CuMnAs thin films, Sci. Rep. **5**, 17079 (2015).

[20] M. Wang, C. Andrews, S. Reimers, O. J. Amin, P. Wadley, R. P. Campion, S. F. Poole, J. Felton, K. W. Edmonds, B. L. Gallagher, A. W. Rushforth, O. Makarovsky, K. Gas, M. Sawicki, D. Kriegner, J. Zubáč, K. Olejník, V. Novák, T. Jungwirth, M. Shahrokhvand *et al.*, Spin flop and crystalline anisotropic magnetoresistance in CuMnAs, Phys. Rev. B **101**, 094429 (2020).

[21] S. F. Poole, L. X. Barton, M. Wang, P. Manuel, D. Khalyavin, S. Langridge, K. W. Edmonds, R. P. Campion, V. Novák, and P. Wadley, Probing the manipulation of antiferromagnetic order in CuMnAs films using neutron diffraction, Appl. Phys. Lett. **121**, 052402 (2022).

[22] P. Wadley, B. Howells, J. Zelezny, C. Andrews, V. Hills, R. P. Campion, V. Novak, K. Olejnik, F. Maccherozzi, S. S. Dhesi, S. Y. Martin, T. Wagner, J. Wunderlich, F. Freimuth, Y. Mokrousov, J. Kuneš, J. S. Chauhan, M. J. Grzybowski, A. W. Rushforth, K. W. Edmonds *et al.*, Electrical switching of an antiferromagnet, Science **351**, 587 (2016).

[23] M. J. Grzybowski, P. Wadley, K. W. Edmonds, R. Beardsley, V. Hills, R. P. Campion, B. L. Gallagher, J. S. Chauhan, V. Novak, T. Jungwirth, F. Maccherozzi, and S. S. Dhesi, Imaging current-induced switching of antiferromagnetic domains in CuMnAs, Phys. Rev. Lett. **118**, 057701 (2017).

[24] S. Reimers, D. Kriegner, O. Gomonay, D. Carbone, F. Krizek, V. Novák, R. P. Campion, F. Maccherozzi, A. Björling, O. J. Amin, L. X. Barton, S. F. Poole, K. A. Omari, J. Michalièka, O. Man, J. Sinova, T. Jungwirth, P. Wadley, S. S. Dhesi, and K. W. Edmonds, Defect-driven antiferromagnetic domain walls in CuMnAs films, Nat. Commun. **13**, 724 (2022).

[25] A. G. Linn, P. Hao, K. N. Gordon, D. Narayan, B. S. Berggren, N. Speiser, S. Reimers, R. P. Campion, V. Novák, S. S. Dhesi, T. K. Kim, C. Cacho, L. Šmejkal, T. Jungwirth, J. D. Denlinger, P. Wadley, and D. S. Dessau, Experimental electronic structure of the electrically switchable antiferromagnet CuMnAs, npj Quantum Mater. **8**, 19 (2023).

[26] F. Máca, J. Masek, O. Stelmakhovych, X. Marti, H. Reichlova, K. Uhlanova, P. Beran, P. Wadley, V. Novak, and T. Jungwirth, Room-temperature antiferromagnetism in CuMnAs, J. Magn. Magn. Mater. **324**, 1606 (2012).

[27] P. Malavi, J. Song, W. Bi, A. Regnat, L. Zhu, A. Bauer, A. Senyshyn, L. Yang, C. Pfleiderer, and J. S. Schilling, High-pressure investigations on the semi-Heusler compound CuMnSb, Phys. Rev. B **98**, 054431 (2018).

[28] K. Endo, T. Ohoyama, and R. Kimura, Antiferromagnetism of CuMnSb, J. Phys. Soc. Jpn. **25**, 907 (1968).

[29] L. Scheffler, J. Werther, K. Gas, C. Schumacher, C. Gould, M. Sawicki, J. Kleinlein, and L. W. Molenkamp, Bulk-like magnetic properties in MBE-grown unstrained, antiferromagnetic CuMnSb, Appl. Phys. Lett. **121**, 012401 (2022).

[30] F. Máca, J. Masek, O. Stelmakhovych, X. Marti, K. Uhlirova, P. Beran, H. Reichlova, P. Wadley, V. Novak, and T. Jungwirth, CuMn-V compounds: A transition from semimetal low-temperature to semiconductor high-temperature antiferromagnets, arXiv:1102.5373.

[31] T. Jeong, R. Weht, and W. E. Pickett, Semimetallic antiferromagnetism in the half-Heusler compound CuMnSb, Phys. Rev. B **71**, 184103 (2005).

[32] M. Doerr, J. Bœuf, C. Pfleiderer, M. Rotter, N. Kozlova, D. Eckert, P. Kerschl, K. H. Müller, and M. Loewenhaupt, Search for half-metallic antiferromagnetism using pulsed magnetic fields: Experimental investigation of Mn_3Si, CuMnSb and PdMnTe, Phys. B: Condens. Matter **346-347**, 137 (2004).

[33] In the CuMnX series, changes of material characteristics are achieved by changing the anion. An analogous possibility is offered by substitution of Cu by other 3*d* transition metal ion. This is the case of half-Heusler CoMnSb [14], NiMnSb [11–13,15], and PtMnSb [68]. The change of the cation does not change the crystal structure, but it induces a crossover of the magnetic phase from AFM to FM together with a change of the electronic structure from semimetallic to half-metallic [16,17].

[34] L. Scheffler, K. Gas, S. Banik, M. Kamp, J. Knobel, H. Lin, C. Schumacher, C. Gould, M. Sawicki, J. Kleinlein, and L. W. Molenkamp, Molecular beam epitaxy of the half-Heusler antiferromagnet CuMnSb, Phys. Rev. Mater. **4**, 114402 (2020).

[35] F. Máca, J. Kudrnovský, V. Drchal, I. Turek, O. Stelmakhovych, P. Beran, A. Llobet, and X. Marti, Defect-induced magnetic structure of CuMnSb, Phys. Rev. B **94**, 094407 (2016).

[36] M. Sawicki, W. Stefanowicz, and A. Ney, Sensitive SQUID magnetometry for studying nanomagnetism, Semicond. Sci. Technol. **26**, 064006 (2011).

[37] K. Gas and M. Sawicki, *In situ* compensation method for high-precision and high-sensitivity integral magnetometry, Meas. Sci. Technol. **30**, 085003 (2019).

[38] P. Stamenov and J. M. D. Coey, Sample size, position, and structure effects on magnetization measurements using second-order gradiometer pickup coils, Rev. Sci. Instrum. **77**, 015106 (2006).

[39] K. Gas, J. Sadowski, and M. Sawicki, Magnetic properties of wurtzite (Ga,Mn)As, J. Magn. Magn. Mater. **533**, 168012 (2021).

[40] H. Du, GPA—geometrical phase analysis software, er-c.org/index.php/software/stem-data-analysis/gpa (2018).

[41] A. Regnat, A. Bauer, A. Senyshyn, M. Meven, K. Hradil, P. Jorba, K. Nemkovski, B. Pedersen, R. Georgii, S. Gottlieb-Schönmeyer, and C. Pfleiderer, Canted antiferromagnetism in phase-pure CuMnSb, Phys. Rev. Mater. **2**, 054413 (2018).

[42] R. H. Forster, G. B. Johnston, and D. A. Wheeler, Studies on the Heusler alloys-III. the antiferro-magnetic phase in the Cu-Mn-Sb system, J. Phys. Chem. Solids **29**, 855 (1968).

[43] M. Endo, H. Kawasoko, S. Soma, K. Yamauchi, M. Kitamura, K. Horiba, H. Kumigashira, N. Kimura, T. Oguchi, T. Sato, and T. Fukumura, Large magnetoresistance of a compensated metal Cu_2Sb correlated with its Fermi surface topology, Phys. Rev. Mater. **5**, 105002 (2021).

[44] R. B. Helmholdt, R. A. de Groot, F. M. Mueller, P. G. van Engen, and K. H. J. Buschow, Magnetic and crystallographic properties of several C1b type Heusler compounds, J. Magn. Magn. Mater. **43**, 249 (1984).

[45] J. Bœuf, C. Pfleiderer, and A. Faißt, Low-temperature properties of the semi-Heusler compound CuMnSb, Phys. Rev. B **74**, 024428 (2006).

[46] H. Mamiya, S. Nimori, M. Ohnuma, I. Nakatani, M. Demura, and T. Furubayashi, Comparison of field-cooled, zero-field-cooled, and thermoremanent magnetization in nanomagnet, random magnet, and bulk ferromagnet, J. Magn. Magn. Mater. **316**, e535 (2007).

[47] L. Gluba, O. Yastrubchak, J. Z. Domagala, R. Jakiela, T. Andrearczyk, J. Żuk, T. Wosinski, J. Sadowski, and M. Sawicki, Band structure evolution and the origin of magnetism in (Ga,Mn)As: From paramagnetic through superparamagnetic to ferromagnetic phase, Phys. Rev. B **97**, 115201 (2018).

[48] A. Navarro-Quezada, M. Aiglinger, B. Faina, K. Gas, M. Matzer, T. Li, R. Adhikari, M. Sawicki, and A. Bonanni, Magnetotransport in phase-separated (Ga,Fe)N with γ'-$Ga_yFe_{4-y}N$ nanocrystals, Phys. Rev. B **99**, 085201 (2019).

[49] K. Gas, A. Krolicka, K. Dybko, P. Nowicki, Z. Khosravizadeh, T. Story, and M. Sawicki, Magnetic constitution of topologically trivial thermoelectric PbTe:Cr, J. Magn. Magn. Mater. **537**, 168154 (2021).

[50] M. Sawicki, D. Chiba, A. Korbecka, Y. Nishitani, J. A. Majewski, F. Matsukura, T. Dietl, and H. Ohno, Experimental probing of the interplay between ferromagnetism and localization in (Ga,Mn)As, Nat. Phys. **6**, 22 (2010).

[51] M. J. Grzybowski, C. Autieri, J. Domagala, C. Krasucki, A. Kaleta, S. Kret, K. Gas, M. Sawicki, R. Bozek, J. Suffczynski, and W. Pacuski, Wurtzite vs. rock-salt MnSe epitaxy: Electronic and altermagnetic properties, Nanoscale **16**, 6259 (2024).

[52] T. Dietl, K. Sato, T. Fukushima, A. Bonanni, M. Jamet, A. Barski, S. Kuroda, M. Tanaka, P. N. Hai, and H. Katayama-Yoshida, Spinodal nanodecomposition in semiconductors doped with transition metals, Rev. Mod. Phys. **87**, 1311 (2015).

[53] P. Hohenberg and W. Kohn, Inhomogeneous electron gas, Phys. Rev. **136**, B864 (1964).

[54] W. Kohn and L. J. Sham, Self-consistent equations including exchange and correlation effects, Phys. Rev. **140**, A1133 (1965).

[55] J. P. Perdew, K. Burke, and M. Ernzerhof, Generalized gradient approximation made simple, Phys. Rev. Lett. **77**, 3865 (1996).

[56] V. I. Anisimov, J. Zaanen, and O. K. Andersen, Band theory and Mott insulators: Hubbard *U* instead of Stoner I, Phys. Rev. B **44**, 943 (1991).

[57] V. I. Anisimov, I. V. Solovyev, M. A. Korotin, M. T. Czyżyk, and G. A. Sawatzky, Density-functional theory and NiO photoemission spectra, Phys. Rev. B **48**, 16929 (1993).

[58] M. Cococcioni and S. de Gironcoli, Linear response approach to the calculation of the effective interaction parameters in the LDA+U method, Phys. Rev. B **71**, 035105 (2005).

[59] Q. ESPRESSO, www.quantum-espresso.org.

[60] A. Ciechan and P. Boguslawski, Transition metal ions in ZnO: Effects of intrashell coulomb repulsion on electronic properties, Opt. Mater. **79**, 264 (2018).

[61] C. E. T. G. da Silva and L. M. Falicov, Theory of magnetic properties of rare earth compounds (localized moments and hybridization effects), J. Phys. C: Solid State Phys. **5**, 63 (1972).

[62] Resistivity is increased by native defects. Indeed, the estimated concentration of antisites involving Cu and Mn sublattices is 1.5 atomic % [35,41].

[63] F. Máca, J. Kudrnovský, V. Drchal, K. Carva, P. Baláž, and I. Turek, Physical properties of the tetragonal CuMnAs: A first-principles study, Phys. Rev. B **96**, 094406 (2017).

[64] J. Kroder, K. Manna, D. Kriegner, A. S. Sukhanov, E. Liu, H. Borrmann, A. Hoser, J. Gooth, W. Schnelle, D. S. Inosov, G. H. Fecher, and C. Felser, Spin glass behavior in the disordered

half-Heusler compound IrMnGa, Phys. Rev. B **99**, 174410 (2019).

[65] C. Kittel, *Introduction to Solid State Physics* (Wiley, New York, NY, 1986).

[66] R. Podloucky and J. Redinger, Density functional theory study of structural and thermodynamical stabilities of ferromagnetic MnX (X = P, As, Sb, Bi) compounds, J. Phys.: Condens. Matter **31**, 054001 (2019).

[67] S. A. Shchukarev, M. P. Morozova, and T. A. Stolyarova, Enthalpy of formation of compounds of manganese with the elements of the main sub-group V, J. Gen. Chem. USSR **31**, 1657 (1961).

[68] P. G. van Engen, K. H. J. Buschow, R. Jongebreur, and M. Erman, PtMnSb, a material with very high magneto-optical Kerr effect, Appl. Phys. Lett. **42**, 202 (1983).